

An ordered, self-assembled nanocomposite with efficient electronic and ionic transport

Tyler J. Quill¹, Garrett LeCroy¹, David M. Halat^{2,3}, Rajendar Sheelamanthula⁴, Adam Marks¹, Lorena S. Grundy^{2,3}, Iain McCulloch^{4,5}, Jeffrey A. Reimer^{2,3}, Nitash P. Balsara^{2,3}, Alexander Giovannitti^{1*}, Alberto Salleo^{1*}, Christopher J. Takacs^{6*}

¹ Department of Materials Science and Engineering, Stanford University, Stanford, CA 94305, United States

² Department of Chemical and Biomolecular Engineering and College of Chemistry, University of California, Berkeley, California 94720, United States

³ Materials Sciences Division and Joint Center for Energy Storage Research, Lawrence Berkeley National Laboratory, Berkeley, California 94720, United States

⁴ Physical Science and Engineering Division King Abdullah University of Science and Technology (KAUST) Thuwal 23955-6900, Saudi Arabia

⁵ Department of Chemistry University of Oxford Oxford, OX1 3TA, UK

⁶ Stanford Synchrotron Radiation Lightsource SLAC National Accelerator Laboratory Menlo Park, CA 94025, United States

A. Giovannitti, A. Salleo

Department of Materials Science and Engineering, Stanford University, Stanford, CA 94305, USA E-mail: asalleo@stanford.edu, ag19@stanford.edu

C.J. Takacs

Stanford Synchrotron Radiation Lightsource SLAC National Accelerator Laboratory Menlo Park, CA 94025, USA E-mail: ctakacs@slac.stanford.edu

Mixed conductors, materials which can efficiently conduct both ionic and electronic species, are an important class of functional solids. Here we demonstrate an organic nanocomposite that forms spontaneously when mixing an organic semiconductor with an ionic liquid and which exhibits efficient room temperature mixed conduction. We use a polymer known to form a semicrystalline microstructure to template ion intercalation into the side-chain domains of the crystallites, which leaves electronic transport pathways intact. The resulting material is thus ordered, exhibiting alternating layers of rigid semiconducting sheets and soft ion conducting layers. This unique dual-network microstructure leads to a dynamic ionic/electronic nanocomposite with liquid-like ionic transport and highly mobile electronic charges. Using a combination of operando X-ray scattering and in-situ spectroscopy, we confirm the ordered structure of the nanocomposite and uncover the mechanisms giving rise to efficient electron transport. These results provide fundamental insights into charge transport in organic semiconductors, while also suggesting a pathway towards future improvements in these nanocomposites.

Mixed conduction - the ability to simultaneously transport both electronic and ionic species - is crucial for a wide array of current and emerging technologies,¹ and mixed conductors can be considered a separate and important class of solids, next to metals, insulators, semiconductors, and ionic conductors. More specifically, there is great interest in solid-state materials where fast ionic concentration changes can deeply modulate electronic and optical properties on timescales commensurate with modern electronics requirements.² The transport of ions and electrons, however, imposes somewhat antithetical requirements on solids, making it difficult to obtain materials which perform both functions well. Critically, there is a lack of fundamental understanding regarding how the coupled dynamics between ions and electrons can be codesigned to promote efficient transport and novel properties for both charged species as compared to pure electronic and ionic conductors. As a result, phase separated composites,³⁻⁵ conjugated polymer – polyelectrolyte blends,^{6,7} or electrically conductive additives mixed into ionic conductors^{8,9} are often used; however, this is far from the optimal as it directly results in lower charge densities. For example, metal oxide cathode materials for battery applications require conductive additives to enhance the electronic conductivity for ion intercalation. The ability to synthesize such composites at the mesoscale and nanoscale is a longstanding grand challenge, where the large number of interfaces per unit volume is functional to obtaining high charge densities.^{1,4}

Organic polymer mixed ionic/electronic conductors (OMIECs) are an emerging class of materials with promise in a wide range of electrochemical devices for energy storage,¹⁰ bioelectronics,¹¹ and neuromorphic computing.¹² While the vast majority of the OMIEC literature uses aqueous electrolytes,¹³ their use with ionic liquids opens opportunities to tailor ionic and electronic functionalities.¹⁴ Ionic liquids, molten salts of charged species without solvent, have become known as designer electrolytes owing to the ability to synthetically tune the

physiochemical properties of these molecules.¹⁵ While these molecules can induce phase separation in conjugated polymer - polyelectrolyte blends,^{16,17} we find that with a judicious choice of materials, ionic liquids spontaneously incorporate into conjugated polymer crystallites as neutral pairs.¹⁸ This infiltration is spontaneous only when the side-chains are designed to be solvated by the ionic liquid. The resulting material is a veritable composite consisting of liquid-like ionically conducting lamellae and semi-rigid electronically conducting lamellae, both structured at the nanoscale while essentially behaving as a single material as if it were a compound.

The mixed conductor nanocomposite presents unique advantages compared to its inorganic counterparts. The self-assembly of the organic semiconductor into lamellae is achieved spontaneously at the nanoscale to provide high volumetric charge densities without the need for the elaborate processing techniques typically required to structure inorganic materials at comparable lengthscales.⁴ We find that the semiconductor lamellae template the nanocomposite formation at the molecular scale as ion swelling occurs only in the softer side-chain domains of the polymer crystallites, preserving this layered structure and leaving the more rigid pathways of electronic transport unperturbed. As a result of this templated self-assembly, ionic and electronic transport pathways coexist within the same unit cell with intimate contact while still enabling efficient conduction of both species simultaneously. This self-assembled nanostructure enables changes in ion composition under an external potential with minimal structural perturbation to the electronically conducting domains which enables us to investigate how electronic charge carriers affect the ordering of the semiconductor. Importantly, ionic conduction is also efficient at room temperature owing to the liquid-like nature of the ionic domains. Thus, the molecularly templated structure, combined with the highly anisotropic nature of transport and volumetric doping of OMIECs leads to optimal ionic and electronic transport properties simultaneously. In addition to

the energy storage and electrocatalysis space, the ionic and electronic transport properties of this nanocomposite opens applications of electrochemical materials in the microelectronics space, where iontronics have recently attracted much attention.^{2,19,20} Finally, the wide materials space available for exploration both on the semiconductor side and the ionic liquid side promises much room for improvement and exploration of different application areas.

To inform synthetic design of these promising nanocomposites for future applications, a fundamental understanding of the charging and transport in these materials must first be established. To date, however, microstructural changes during OMIEC operation are largely unknown. Indeed, despite notable progress,^{21–26} simultaneously measuring carrier density and conductivity while characterizing structural changes (for example by grazing incidence X-ray scattering) has proven challenging. Thus, studies providing mechanistic insights and rigorous structure-property relationships have been limited. To fill this gap, we developed *operando* measurements that quantify structural changes during electrochemical charging and correlate the evolving microstructure to simultaneously measured electronic transport properties (such as hole mobility). We use these insights to reveal which semiconductor microstructure is most favorable for charge transport, thereby suggesting a path towards future improvements in these nanocomposites.

Monitoring Structure with Operando X-ray Scattering

To study the paired electrical and structural dynamics in the mixed conductor nanocomposite, we use a porous, insulating ceramic substrate for operando X-ray scattering. The ceramic substrate performs several functions: it serves as a reservoir of 1-Ethyl-3-methylimidazolium bis(trifluoromethylsulfonyl)imide (EMIM:TFSI), acts as a suitable substrate

for grazing-incidence scattering (minimal overlap with the OMIEC, **Fig. 1**, **Supplementary Fig. 1**), and its insulating nature limits parasitic currents and side reactions during charging/discharging the OMIEC poly(2-(3,3'-bis(2-(2-(2-methoxyethoxy)ethoxy)ethoxy)-[2,2'-bithiophen]-5-yl)thieno [3,2-b]thiophene) (p(g2T-TT)) (**Fig. 1b**, **Supplementary Fig. 2**). This design enables high quality electrochemical characterization to be performed on polymer thin films at synchrotron beamlines, demonstrated by the operando cyclic voltammogram (CV) in **Fig. 1c**.

Upon forming the nanocomposite by permeating p(g2T-TT) with EMIM:TFSI, the most conspicuous change is in the (100) peak, which corresponds to the lamellar stacking distance. This spacing expands by 5.3 Å (31%) due to EMIM:TFSI molecules spontaneously entering the side-chain lamellae. This expansion is commensurate with the ion dimensions.²⁷ Based on the swelling and molar volumes of the components, we estimate there is on average one anion-cation pair per monomer in the mixed conductor nanocomposite (**Table S1**). Surprisingly, after the initial intercalation of ions into the polymer structure, electrochemical charging of the semiconductor does not result in significant expansions of the lamellar stacking distance, and in fact a modest contraction is observed (**Supplementary Fig. 4**). We thus attribute this contraction to cation expulsion needed to maintain charge neutrality of the nanocomposite following polymer oxidation. Notably, the restructuring of ionic liquid gated OMIEC materials differ greatly from aqueous systems, where hydrated anions entering the crystallites during electrochemical charging cause expansions of the (*h*00) planes.²⁸

We represent the evolution of the material's structure during the CV in the form of a heat map where the scattering is collected every second and shown as a column of pixels (**Fig. 2**). By measuring the injected charge during the CV (**Supplementary Fig. 5**), the carrier density in the

semiconductor can be quantitatively correlated to structural changes in the nanocomposite. The modulation of the (100) peak area is perfectly synchronized with the charge carrier density changes in the film (**Fig. 2a**), indicating that electrochemical doping is responsible for the observed changes (**Supplementary Note 1**) and highlighting the ideal reversibility of the ion insertion/expulsion processes. The (010) peak, corresponding to the π -stacking of the rigid backbones, undergoes a modest contraction upon charging (**Fig. 2b**). The π -stacking contraction appears most rapid at lower carrier densities when the first charges are added and exhibits minimal change towards the maximum carrier densities (and most positive electrochemical potentials). The peak shift is also accompanied by small intensity increases, attributed to greater crystallinity due to the planarization of conjugated backbone units ensuing polaron formation.

To investigate electronic transport in the nanocomposite, we operate the film as the channel of an electrochemical transistor by patterning source and drain electrodes on the insulating substrate (**Fig. 3a**). The electrochemical potential of the sample was varied relative to the reference electrode while the conductivity was measured with a small (50 mV) bias between source and drain.²⁹ Thus, differential and average carrier mobilities can be determined from conductivity changes following known increases in carrier density in the film (**Fig. 3b**). In agreement with CV measurements, the area of the lamellar stacking peak increases linearly with carrier density, and the greatest contraction in the π -stacking distance occurs at potentials just above the threshold of the transistor, indicating that the initial carriers produce larger changes in the structure of the crystallites (**Fig. 3c-d**). The differential hole mobility reaches a peak at 0.3-0.4 V which aligns well with the peak transconductance, confirming that this peak is governed by transport rather than capacitance.³⁰ Interestingly, the differential hole mobility peaks at a potential where the π -stacking

of the material shows minimal contraction upon charging. The continued evolution of the (100) peak area indicates charging of crystallites, but the addition of these high mobility carriers do not result in significant π -stacking strains.

Evolution of Polaron-Induced Ordering in the Polymer

Operando X-ray scattering provides information about structural transformations of the crystallites upon charging. Spectroelectrochemistry on the other hand reveals information about where the injected charges reside in the microstructure, for example disordered regions vs. aggregates, providing complementary information. To this end, we employ electrochemical charge modulation spectroscopy (eCMS) in the visible-near-infrared region to measure changes to both the aggregate and amorphous absorption in p(g2T-TT). As the film potential is stepped from a neutral state to an oxidized state, the addition of charge carriers bleaches the π - π^* absorption (**Supplementary Fig. 6**). The difference between subsequent spectra is the absorption from the regions in the material where newly added charge carriers reside, shown in **Fig. 4a**. Fitting the vibronic features of these differential spectra across a range of electrochemical potentials (**Supplementary Note 2**) provides insights into the local environment experienced by charge carriers at specific energies in the density of states (DOS). Indeed, the ratio in oscillator strength of the first two vibronic features (the 0-0/0-1 ratio) is related to the relative amount of *intrachain* and *interchain* delocalization of excitons created upon photoexcitation.³¹ These exciton delocalization lengths are proxies for order: a chain with more intrachain order (more J-like) will lead to the formation of excitons that exhibit reduced interchain delocalization (less H-like).^{32,33} Hence, the degree of intrachain coupling has been taken as a measure of crystalline quality: a

greater intrachain delocalization of the exciton is indicative of more ordered chains in higher quality crystallites.³⁴

As the electrochemical potential is increased, the absorption of neutral (unbleached) aggregates in the film decreases steadily after the oxidation onset, as most (~84%) of the injected charge carriers go to aggregates rather than amorphous regions (**Fig. 4b**, **Supplementary Fig. 7**). As carriers are added deeper into the DOS, we find that newly added carriers populate increasingly J-like chains, as reported in P3HT.³⁵ This is evidenced by a blueshift in the E_{0-0} , as well as the 0-0/0-1 ratio which rises above unity.^{36,37} Such changes are characteristic of chains with planar backbones which allow for intrachain delocalization of excitons.^{34,37} The transition to populating more J-like aggregates coincides with an increase in the coherence length of the π -stacking peak, indicating increased order within the crystallites (**Fig. 4b**). Recall that the largest contraction in the π -stacking distance was observed at lower carrier densities (**Fig. 3**) when newly added carriers still populate chains that possess considerable H-aggregate character and are thus more disordered. We conclude that these initial charge carriers result in chain straightening and planarization in lower quality crystallites, which has two effects: i) it decreases π -stacking distance and ii) it increases the π -stacking coherence length, resulting in an overall enhancement of crystalline order. This change increases the mobility of the subsequent carriers as they populate aggregates with more pronounced J-aggregate character since the chain-straightened crystallites possess higher intrachain order and longer conjugation lengths (**Supplementary Note 3**). Thus, we conclude that transport becomes more efficient at higher carrier densities because the initial carriers induce intrachain order in neighboring chains, which increases the mobility of subsequent carriers.

Probing Ion Dynamics in the Nanocomposite

To investigate the nature of the ions located within the crystalline lamellae, we performed ^1H and ^{19}F pulsed field gradient (PFG) NMR spectroscopy to directly measure ion diffusion. Self-diffusion coefficients in the neat ionic liquid were measured at 25 °C and determined to be 5.6 and $3.4 \times 10^{-7} \text{ cm}^2/\text{s}$ for the cation (EMIM^+) and anion (TFSI^-), respectively (**Supplementary Fig. 8**). Similar measurements were then performed on an oriented film of the nanocomposite to characterize the dynamics of the ions confined between the semiconductor lamellae. Analysis of the diffusivity measurements by fitting attenuation data to the Stejskal-Tanner equation revealed two-component diffusion for both the cation and anion (**Supplementary Fig. 9**).^{38,39} The diffusivities of the faster-diffusing components for both cation and anion match the values of the neat ionic liquid, which we attribute to excess ionic liquid on the surface or between wrapped layers. The slower-diffusing component corresponds to ionic liquid confined within the nanocomposite, which is highly mobile even at 25 °C ($D_{\text{EMIM}} = 9 \times 10^{-8} \text{ cm}^2/\text{s}$ and $D_{\text{TFSI}} = 4.3 \times 10^{-8} \text{ cm}^2/\text{s}$).⁴⁰ In previous work, cation and anion diffusivities for an ionic liquid (PEt_4BF_4) confined within the carbon nanopores of a supercapacitor electrode were reduced by more than 100x, with strong dependence on pore size.⁴¹ The larger characteristic spacing in this system ($\sim 2.2 \text{ nm}$) and interactions with the side-chains likely contribute to the enhanced ion mobility, providing efficient ionic transport at room temperature even though, at most, only a few molecular layers of ionic liquid are present between each semiconductor sheet. We further note that semiconductor side-chain length (and thus lamellar spacing) can be synthetically designed, which offers intriguing opportunities to further enhance ionic transport in these materials.

Charge Transport Insights

We showed the formation of polymer-ionic liquid compounds that are promising materials at the nexus of electrochemistry and solid-state physics. Starting with a polymer which forms an ordered semicrystalline microstructure, we observe that the spontaneous infiltration of the ionic liquid into the polymer crystallites does not destroy the ordered microstructure. Such spontaneous swelling does not occur when non-polar alkyl side-chains are used (**Supplementary Fig. 10**), so ion insertion in such polymers produces significant structural perturbations which impose kinetic barriers.^{42,43} Thus, the composite system we investigate here is unique in this respect, highlighting the modularity of synthetic design where independently designed backbones and side-chains can be combined.⁴⁴

The complete permeation of the polymer with ionic liquid has important consequences for both ion and electron transport. Because of the high ionic density within the crystallites, the insertion or expulsion of an ion during charging need not involve any long-range ionic motion or significant structural deformation. Indeed, this process can be viewed as the reversible formation of an “ionic vacancy” or an “ionic interstitial” in the already formed polymer/ionic liquid composite. This process can occur quickly by ion-ion interactions at the interface with the electrolyte or amorphous domains. The stabilization afforded by the large ion density combined with the material’s nanostructured nature enables charge storage densities ($\sim 20 \text{ C.cm}^{-3}$) orders of magnitude higher than other artificial mixed conductors.³ Furthermore, since the ionic liquid mostly retains its liquid-like transport properties within the nanocomposite, these short-range diffusion processes can be fast, as corroborated by PFG-NMR. In this context, it has already been observed that artificial synapses made with our composites exhibit high speed switching down to the ns domain, not limited by fundamental materials properties but rather by device design.¹⁴ This is a case where decreased ion transit distances can lead to faster operation, as has been shown for

internal-ion gated transistors.⁴⁵ This switching mechanism suggests that polymer/ionic liquid composites hold great promise for fast-switching iontronic devices and beyond, thus realistically opening the optoelectronics space to electrochemical materials.

The lack of significant structural deformation on the other hand ensures that electronic transport is not impeded upon ion intercalation. In fact, we find that hole mobility is high in these composites and that charging gives rise to a sharp increase in carrier transport. The explanation for such observation is made possible by our multimodal study. We observe that the first carriers are introduced to crystallites with relatively disordered chains that form H-like aggregates. Interestingly, the relatively low carrier mobility observed in these conditions ($\sim 0.1 \text{ cm}^2/\text{V.s}$) is similar to that observed in field-effect devices and indeed occurs at similar charge densities ($\sim 1\text{-}2 \times 10^{19} \text{ cm}^{-3}$). Evidence of the initial disorder of these chains is given by the π -stacking contraction upon charging and subsequent increase in coherence length, whereby it is known that charged chains are straighter and thus prone to better packing. The high charge densities achievable by electrochemical gating enables populating of chains characterized by increased intrachain order in the crystallites. These more planar chains allow for higher mobility, up to $1 \text{ cm}^2/\text{V.s}$, and their degree of order is such that the addition of charges no longer appreciably affects π -stacking. Thus we conclude that the key to high mobility in this conjugated polymer is access to chains exhibiting more intrachain order. In electrochemical doping, these chains are dynamically created by the initial charge carriers. While it is often stated that high mobility polymers should exhibit interchain delocalization of polarons, our results indicate that high mobility is dependent on efficient 1D transport along single chains. Being able to modulate charge density with minimal structural changes makes this result unambiguous.

Outlook

In summary, we show that ionic liquids and conjugated polymers can spontaneously form nanostructured mixed conductors that exhibit reversible electrochemical doping and electronic transport modulation. These composites exhibit efficient electronic and ionic transport at room temperature; they are effectively bulk mixed conductors due to the intimate contact between ionically and electronically conducting domains at the nanoscale. Using the multimodal characterization techniques developed, we reveal that the addition of charge carriers induces subtle changes to polymer conformation within the crystallites. These changes enhance intrachain ordering, thereby increasing the mobility of the subsequent carriers. Thus, such operando characterization allows us to uncover the mechanisms underlying the surprisingly high hole mobility observed in polymeric mixed conductors and the origin of the strong charge density dependence of transport. In a broader context, this electrochemically active nanocomposite offers exciting possibilities at the nexus of solid-state chemistry and electronics due to the ability to achieve fast and deep modulation up to high electronic carrier densities in the semiconductor lamellae. Combined with the ability to synthetically design both the electronic and ionic domains of the nanocomposite, there exists a large design space for the synthesis of materials families exhibiting fast modulation of a wide range of electronic, optical, thermal and even mechanical properties.

Acknowledgements

The authors thank Lee Richter for helpful discussions regarding X-ray scattering results, and Edward Barks for assistance with ceramic polishing. T.J.Q. and G.L. acknowledge support from the National Science Foundation Graduate Research Fellowship Program under grant DGE-

1656518. This material is based upon work supported by the U.S. Department of Energy, Office of Science, Office of Workforce Development for Teachers and Scientists, Office of Science Graduate Student Research (SCGSR) program. The SCGSR program is administered by the Oak Ridge Institute for Science and Education for the DOE under contract number DE-SC0014664. A.G. and A.S. acknowledge funding from the TomKat Center for Sustainable Energy at Stanford University. A.S. gratefully acknowledges financial support from the National Science Foundation Award # DMR 1808401. Use of the Stanford Synchrotron Radiation Lightsource, SLAC National Accelerator Laboratory, is supported by the U.S. Department of Energy, Office of Science, Office of Basic Energy Sciences under Contract No. DE-AC02-76SF00515. Part of this work was performed at the Stanford Nano Shared Facilities (SNSF), supported by the National Science Foundation under award ECCS-2026822. A.S. and T.J.Q. acknowledge financial support from the National Science Foundation and the Semiconductor Research Corporation, E2CDA Award #1739795. We thank Dr. Hasan Celik and UC Berkeley's NMR facility in the College of Chemistry (CoC-NMR) for spectroscopic assistance; the instrument used in this work is supported by the National Science Foundation under Grant No. 2018784. D.M.H. acknowledges support from the Joint Center for Energy Storage Research, an Energy Innovation Hub funded by the U.S. Department of Energy, Office of Science, Basic Energy Sciences.

Author Contributions: T.J.Q, C.J.T, A.S, and A.G. conceived the study. T.J.Q. and C.J.T. performed operando X-ray scattering experiments and analyzed the data. T.J.Q and G.L. carried out spectroscopic measurements and G.L performed exciton fitting. D.M.H. performed PFG NMR measurements under the supervision of J.A.R and N.P.B.. R.S. synthesized p(g2T-TT) under the

supervision of I.M.. T.J.Q, A.G, and A.S wrote the manuscript and all authors contributed to manuscript preparation and editing.

Competing : The authors declare no competing interests.

Figures:

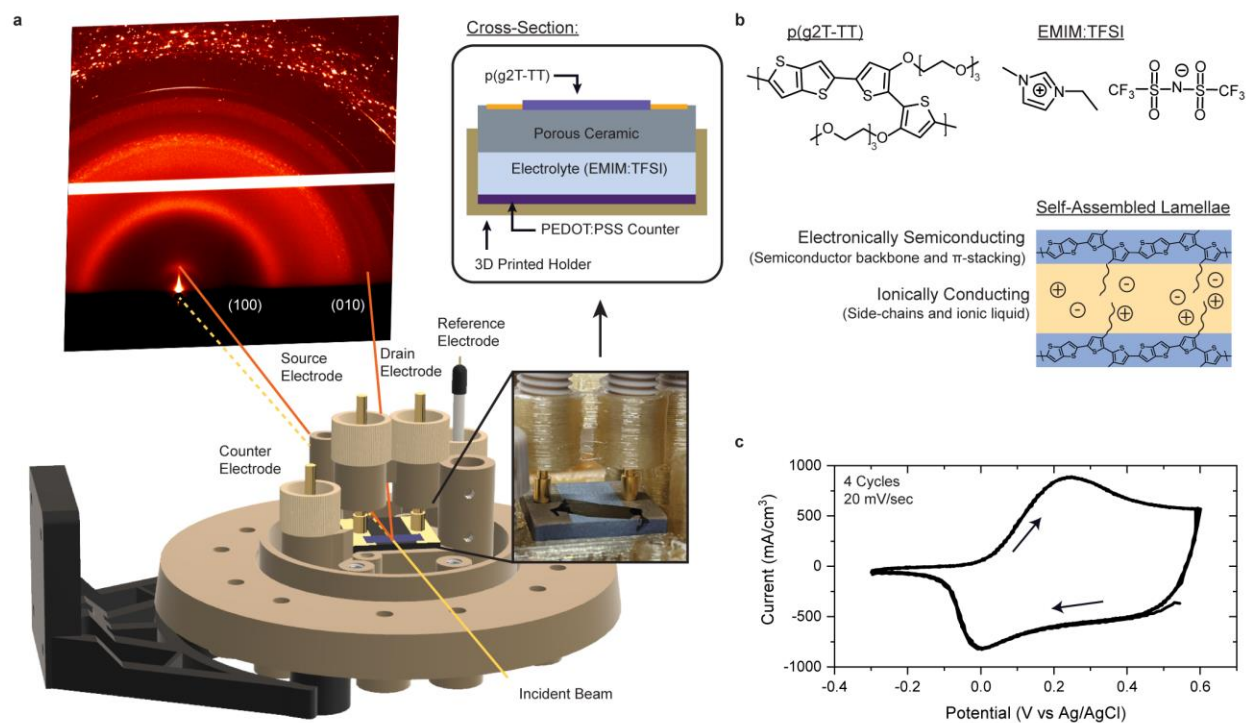


Figure 1: Characterization of nanocomposite structure. (a) Schematic of electrochemical cell used for operando X-ray scattering measurements. (b) Chemical structures of the components and schematic of the nanocomposite structure. (c) Cyclic Voltammogram (CV) of the system taken during operando X-ray characterization, with the scan direction shown by the arrows.

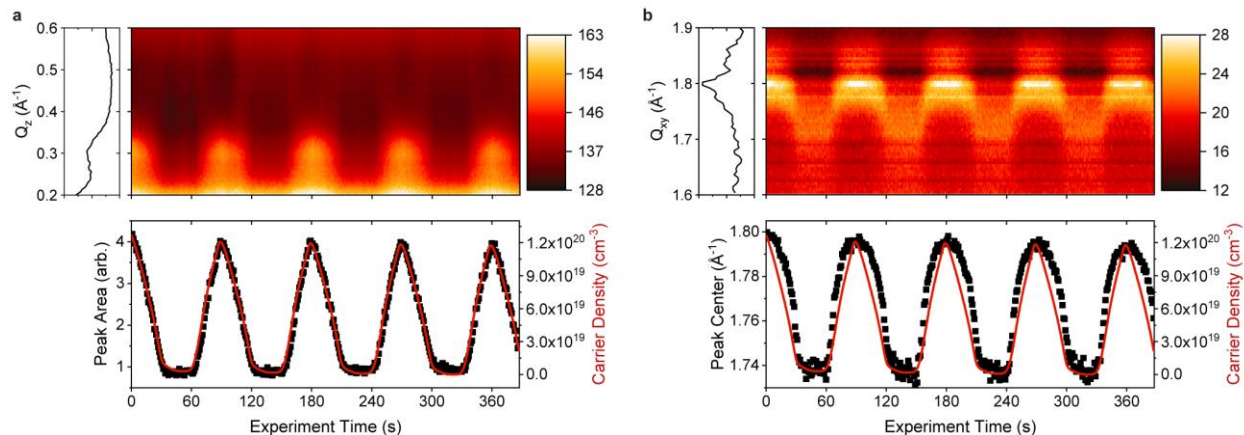


Figure 2: Structural evolution of the material under electrochemical charging. The (a) lamellar stacking peak area and (b) π -stacking peak center of p(g2T-TT) over the course of a CV. The scan rate was 20 mV/s and the potential range was -0.3 V to 0.6 V vs Ag/AgCl. The colorbar on the right of the heatmaps displays the intensity scale used to show the peak changes during the experiment, and an initial scattering lineout is shown on the left. Fits were performed for each lineout and are shown in the bottom panel. The carrier density in the film throughout the duration of the CV, displayed in red, is overlaid with the relevant scattering fits.

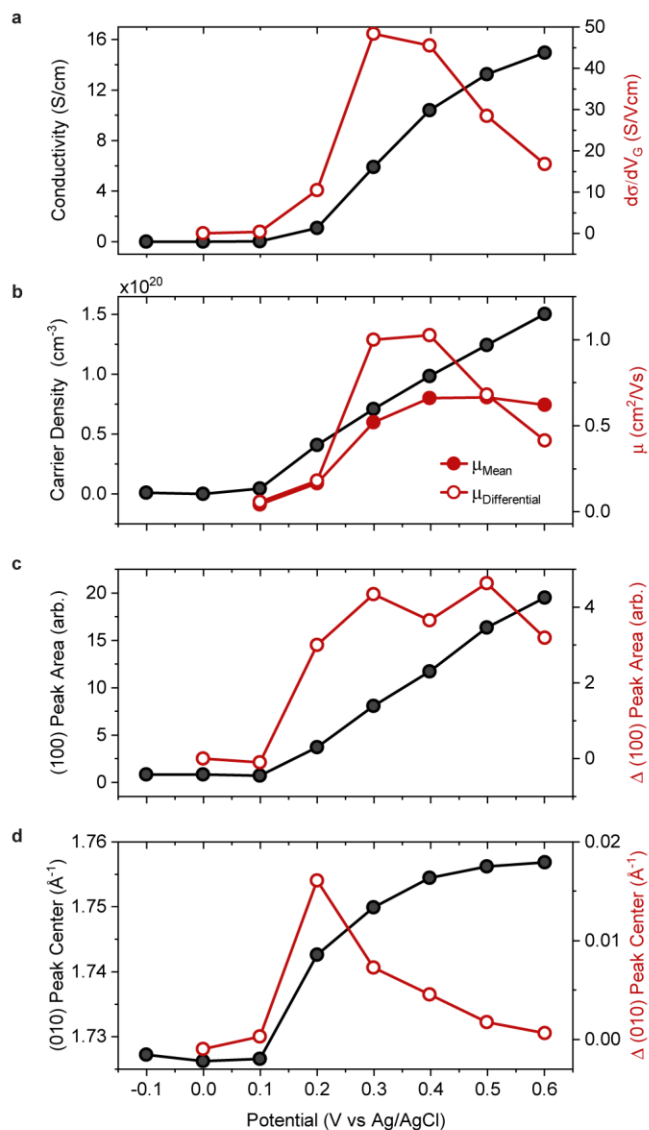


Figure 3: Operando OECT transfer curve. (a) Conductivity (black) and $d\sigma/dV_G$ (the conductivity analogue of transconductance) (red) (b) Charge carrier density (black) and corresponding hole mobility (red). The “differential” mobility (open symbols) is the mobility of newly added carriers at each potential step, given by $\Delta\sigma/(e\Delta p)$, whereas the “mean” mobility (solid symbols) is the average mobility of all carriers, given by $\sigma/(ep)$. Peak fits of the (c) lamellar stacking peak area and (d) π -stacking peak center are shown in black, and the relative changes from the previous electrochemical potential are shown in red. The film’s electrochemical potential (x-axis) is reported relative to an Ag/AgCl reference electrode.

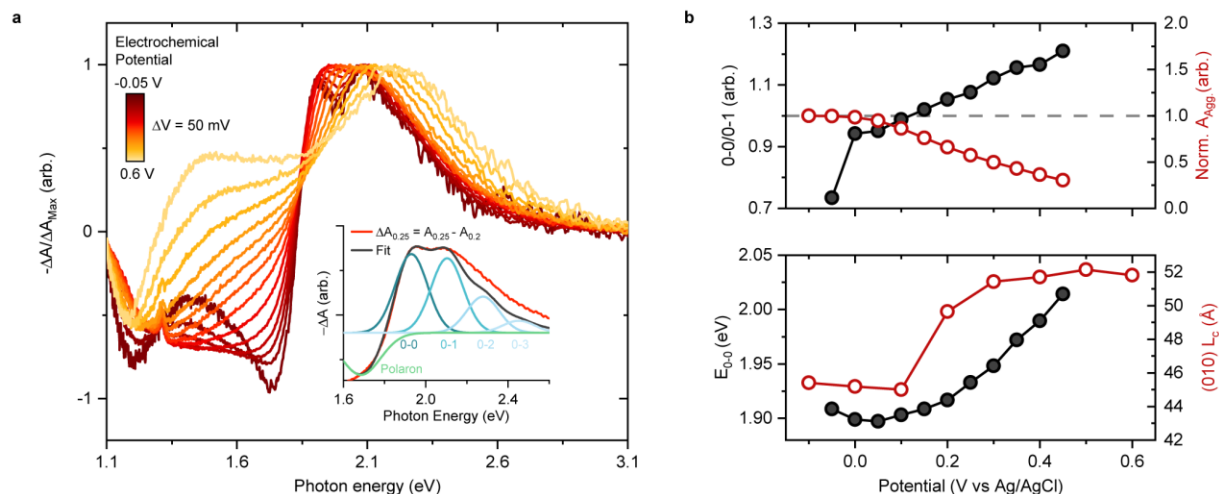


Figure 4: Electrochemical charge modulation spectroscopy. (a) Differential visible-near-infrared absorption spectra at different electrochemical potentials (colorbar). Spectra were normalized to the bleaching of the π - π^* transition for qualitative comparison of spectral shape. A representative fit of the charge modulated spectra is inset, including polaron and vibronic (0-0, 0-1, 0-2, 0-3) absorptions. (b) Results from fitting the differential spectra showing the 0-0/0-1 ratio for newly bleached chains (black) and the absorption of unbleached aggregates (red) normalized to the initial value (top). The 0-0 transition energy (E_{0-0}) (black) and coherence length (L_c) of the (010) scattering peak (red), taken from the operando transfer curve (bottom). Electrochemical potentials are reported relative to an Ag/AgCl reference electrode. The film's potential was stepped from -0.1 V to 0.6 V vs Ag/AgCl in 50 mV steps, and spectra and corresponding fits are reported at the endpoint of the potential step (inset).

References

1. Maier, J. Nanoionics: ion transport and electrochemical storage in confined systems. *Nat. Mater.* **4**, 805–815 (2005).
2. Bisri, S. Z., Shimizu, S., Nakano, M. & Iwasa, Y. Endeavor of Iontronics: From Fundamentals to Applications of Ion-Controlled Electronics. *Advanced Materials* **29**, (2017).
3. Chen, C. C., Fu, L. & Maier, J. Synergistic, ultrafast mass storage and removal in artificial mixed conductors. *Nature* **536**, 159–164 (2016).
4. Sata, N., Eberman, K., Eberl, K. & Maier, J. Mesoscopic fast ion conduction in nanometre-scale planar heterostructures. *Nat. 2000 4086815* **408**, 946–949 (2000).
5. Casado, N., Zendegi, S., Olmo, R. Del, Dominguez-Alfaro, A. & Forsyth, M. Tuning Electronic and Ionic Conductivities in Composite Materials for Electrochemical Devices. *ACS Appl. Polym. Mater.* **3**, 1777–1784 (2021).
6. del Olmo, R., Mendes, T. C., Forsyth, M. & Casado, N. Mixed ionic and electronic conducting binders containing PEDOT:PSS and organic ionic plastic crystals toward

- carbon-free solid-state battery cathodes. *J. Mater. Chem. A* 19777–19786 (2022). doi:10.1039/d1ta09628a
7. Olmo, R. Del, Casado, N., Olmedo-Martínez, J. L., Wang, X. & Forsyth, M. Mixed ionic-electronic conductors based on PEDOT:PolyDADMA and organic ionic plastic crystals. *Polymers (Basel)*. **12**, 1–18 (2020).
 8. Chen, H. *et al.* Exploring Chemical, Mechanical, and Electrical Functionalities of Binders for Advanced Energy-Storage Devices. *Chem. Rev.* **118**, 8936–8982 (2018).
 9. Lopez, J., Mackanic, D. G., Cui, Y. & Bao, Z. Designing polymers for advanced battery chemistries. *Nat. Rev. Mater.* **4**, 312–330 (2019).
 10. Tan, S. T. M. *et al.* Redox-Active Polymers Designed for the Circular Economy of Energy Storage Devices. *ACS Energy Lett.* **6**, 3450–3457 (2021).
 11. Cea, C. *et al.* Enhancement-mode ion-based transistor as a comprehensive interface and real-time processing unit for in vivo electrophysiology. *Nat. Mater.* **19**, 679–686 (2020).
 12. Tuchman, Y., Quill, T. J., LeCroy, G. & Salleo, A. A Stacked Hybrid Organic/Inorganic Electrochemical Random-Access Memory for Scalable Implementation. *Adv. Electron. Mater.* 2100426 (2021). doi:10.1002/aelm.202100426
 13. Paulsen, B. D., Tybrandt, K., Stavrinidou, E. & Rivnay, J. Organic mixed ionic–electronic conductors. *Nature Materials* **19**, 13–26 (2020).
 14. Melianas, A. *et al.* Temperature-resilient solid-state organic artificial synapses for neuromorphic computing. *Sci. Adv.* **6**, (2020).
 15. Lei, Z., Chen, B., Koo, Y. M. & Macfarlane, D. R. Introduction: Ionic Liquids. *Chem. Rev.* **117**, 6633–6635 (2017).
 16. Wu, X. *et al.* Ionic-Liquid Doping Enables High Transconductance, Fast Response Time, and High Ion Sensitivity in Organic Electrochemical Transistors. *Adv. Mater.* **31**, 1–9 (2019).
 17. Wu, X. *et al.* Ionic-Liquid Induced Morphology Tuning of PEDOT:PSS for High-Performance Organic Electrochemical Transistors. *Adv. Funct. Mater.* **32**, (2022).
 18. Quill, T. J. *et al.* Ion Pair Uptake in Ion Gel Devices Based on Organic Mixed Ionic–Electronic Conductors. *Adv. Funct. Mater.* 2104301 (2021). doi:10.1002/ADFM.202104301
 19. Hou, Y. & Hou, X. Bioinspired nanofluidic iontronics. *Science (80-.)*. **373**, 628–629 (2021).
 20. Chun, H. & Chung, T. D. Iontronics. *Annu. Rev. Anal. Chem.* **8**, 441–462 (2015).
 21. Bischak, C. G. *et al.* A Reversible Structural Phase Transition by Electrochemically-Driven Ion Injection into a Conjugated Polymer. *J. Am. Chem. Soc.* **142**, 7434–7442 (2020).
 22. Thomas, E. M. *et al.* X-Ray Scattering Reveals Ion-Induced Microstructural Changes

- During Electrochemical Gating of Poly(3-Hexylthiophene). *Adv. Funct. Mater.* **28**, 1803687 (2018).
23. Paulsen, B. D. *et al.* Electrochemistry of Thin Films with In Situ/Operando Grazing Incidence X-Ray Scattering: Bypassing Electrolyte Scattering for High Fidelity Time Resolved Studies. *Small* **17**, 2103213 (2021).
 24. Flagg, L. Q. *et al.* In Situ Studies of the Swelling by an Electrolyte in Electrochemical Doping of Ethylene Glycol-Substituted Polythiophene. *ACS Appl. Mater. Interfaces* (2022). doi:10.1021/acsami.2c06169
 25. Thelen, J. L. *et al.* Relationship between Mobility and Lattice Strain in Electrochemically Doped Poly(3-hexylthiophene). *ACS Macro Lett.* **4**, 1386–1391 (2015).
 26. Zhang, S., Beach, E., Anastas, P. T., Pfefferle, L. D. & Osuji, C. O. Self-assembly of supramolecular complexes of charged conjugated polymers and imidazolium-based ionic liquid crystals. *Giant* **9**, 100088 (2022).
 27. Largeot, C. *et al.* Relation between the ion size and pore size for an electric double-layer capacitor. *J. Am. Chem. Soc.* **130**, 2730–2731 (2008).
 28. Cendra, C. *et al.* Role of the Anion on the Transport and Structure of Organic Mixed Conductors. *Adv. Funct. Mater.* **29**, 1807034 (2019).
 29. Hulea, I. N. *et al.* Wide energy-window view on the density of states and hole mobility in poly(p-phenylene vinylene). *Phys. Rev. Lett.* **93**, 16–19 (2004).
 30. Friedlein, J. T. *et al.* Influence of disorder on transfer characteristics of organic electrochemical transistors. *Appl. Phys. Lett.* **111**, (2017).
 31. Chang, X., Balooch Qarai, M. & Spano, F. C. HJ-aggregates of donor–acceptor–donor oligomers and polymers. *J. Chem. Phys.* **155**, 034905 (2021).
 32. Clark, J., Silva, C., Friend, R. H. & Spano, F. C. Role of intermolecular coupling in the photophysics of disordered organic semiconductors: Aggregate emission in regioregular polythiophene. *Phys. Rev. Lett.* **98**, 1–4 (2007).
 33. Spano, F. C. Modeling disorder in polymer aggregates: The optical spectroscopy of regioregular poly(3-hexylthiophene) thin films. *J. Chem. Phys.* **122**, (2005).
 34. Clark, J., Chang, J. F., Spano, F. C., Friend, R. H. & Silva, C. Determining exciton bandwidth and film microstructure in polythiophene films using linear absorption spectroscopy. *Appl. Phys. Lett.* **94**, 3–6 (2009).
 35. Harris, J. K., Neelamraju, B. & Ratcliff, E. L. Intersystem Subpopulation Charge Transfer and Conformational Relaxation Preceding in Situ Conductivity in Electrochemically Doped Poly(3-hexylthiophene) Electrodes. *Chem. Mater.* **31**, 6870–6879 (2019).
 36. Brown, P. J. *et al.* Effect of interchain interactions on the absorption and emission of poly(3-hexylthiophene). *Phys. Rev. B - Condens. Matter Mater. Phys.* **67**, 1–16 (2003).
 37. Spano, F. C. & Silva, C. H- and J-aggregate behavior in polymeric semiconductors. *Annu. Rev. Phys. Chem.* **65**, 477–500 (2014).

38. Stejskal, E. O. & Tanner, J. E. Spin diffusion measurements: Spin echoes in the presence of a time-dependent field gradient. *J. Chem. Phys.* **42**, 288–292 (1965).
39. Sinnaeve, D. The Stejskal-Tanner equation generalized for any gradient shape-An overview of most pulse sequences measuring free diffusion. *Concepts Magn. Reson. Part A Bridg. Educ. Res.* **40 A**, 39–65 (2012).
40. Hoarfrost, M. L., Tyagi, M. S., Segalman, R. A. & Reimer, J. A. Effect of confinement on proton transport mechanisms in block copolymer/ionic liquid membranes. *Macromolecules* **45**, 3112–3120 (2012).
41. Forse, A. C. *et al.* Direct observation of ion dynamics in supercapacitor electrodes using in situ diffusion NMR spectroscopy. *Nat. Energy* **2**, 1–7 (2017).
42. Guardado, J. O. & Salleo, A. Structural Effects of Gating Poly(3-hexylthiophene) through an Ionic Liquid. *Adv. Funct. Mater.* **27**, (2017).
43. Lee, J. *et al.* Ion gel-gated polymer thin-film transistors: Operating mechanism and characterization of gate dielectric capacitance, switching speed, and stability. *J. Phys. Chem. C* **113**, 8972–8981 (2009).
44. Bronstein, H., Nielsen, C. B., Schroeder, B. C. & McCulloch, I. The role of chemical design in the performance of organic semiconductors. *Nature Reviews Chemistry* **4**, 66–77 (2020).
45. Spyropoulos, G. D., Gelinas, J. N. & Khodagholy, D. Internal ion-gated organic electrochemical transistor: A building block for integrated bioelectronics. *Sci. Adv.* **5**, eaau7378 (2020).

Methods

Cell fabrication: The operando cell was designed using Fusion360 (Autodesk) and printed from 3DX-TECH PEKK-A on an Intamsys Funmat HT printer. The entrance and exit windows of the cell consisted of 8 μm aluminum foils (MTI Corporation) and were sealed with Kapton tape.

The scattering from these windows is at sufficiently high q that no scattering overlaps with the areas of interest. Kapton tape was used to seal any openings and to provide optical access during alignment.

Substrate preparation: Porous ceramic substrates (Newark) were cleaned in acetone and polished by hand using diamond lapping paper (McMasterCarr). Gold contacts were evaporated onto the frits using a thermal evaporator in a Nitrogen glovebox.

Film transfer: p(g2T-TT), synthesized as previously reported,⁴⁶ was dissolved in chloroform (1 mg/mL) and blade coated on a Si wafer coated with a poly(diallyldimethylammonium bis(trifluoromethanesulfonyl)imide) (polyDADMAC TFSI) lift-off-layer (spun 1000 rpm, 10 mg/mL). The blade coated film was lifted off the Si substrate in acetone and transferred to the porous ceramic.

Operando X-ray scattering: Grazing incidence wide angle X-ray scattering measurements of p(g2T-TT) were performed at the Stanford Synchrotron Radiation Light source on beamline 10-2 using an incident photon energy of 12 keV using a focused beam approximately 50 μm in height. An Eiger 1M detector was mounted on a two-theta arm at a distance 152 mm away from the sample at an angle of 10 degrees. Measurements were taken at an incident angle of 0.5 degrees at ambient temperature. Out-of-plane (Q_z) and in-plane (Q_{xy}) lineouts were taken from cake-slices from $\chi = -20$ to 20 degrees and 60 to 87 degrees with respect to the Q_z direction, respectively. Small-angle scattering between $\chi = -5$ and 5 degrees was excluded from the out-of-plane lineouts. Peaks were fit to gaussian-lorentzian lineshapes using the lmfit package in python. To isolate the π -stacking peak for fitting, out-of-plane lineouts were subtracted from the in-plane lineouts to remove the isotropic scattering from the substrate. X-ray scattering data was reduced in python using the open source pyFAI and pygix modules.^{47,48} A forked version of the pygix module was used (available at <https://github.com/ctakacs/pygix>) for compatibility with python3.

Operando electrochemistry: Electrochemical measurements were taken on a two-channel Biologic SP-300 potentiostat in a 3-electrode setup with a leakless Ag/AgCl reference electrode

(eDAQ) and a PEDOT:PSS (Clevios PH1000) counter electrode. EMIM:TFSI (Iolitec) was stored in a nitrogen glovebox prior to use. PEDOT:PSS was prepared as previously described¹⁴ and drop casted on a conductive carbon paper (P75, Fuel Cell Store) to form a high capacitance counter electrode. CV experiments were performed on unpatterned ceramic substrates, or by connecting the source and drain electrodes of a patterned substrate to the working electrode of the potentiostat. Operando transistor measurements were performed by separately biasing the source and drain electrodes using the dual-channel potentiostat as a bipotentiostat, still in a 3-electrode setup (namely, with separate counter and reference electrodes). Carrier density was calculated from the injected charge over the course of the CV or transfer curve and film volume. The thicknesses were measured after experiments were performed and thus correspond to the swollen state of the material.

Electrochemical charge modulation spectroscopy: Spectroelectrochemical measurements were performed using a home-built spectrometer with an Ocean Optics light source (Tungsten Halogen Light Sources) and detector (Red Tide Ocean Optics). A quartz cuvette with a 3D-printed holder was used to conduct measurements in transmission mode. The cuvette was capped with a 3D-printed cap and purged with argon to remove ambient oxygen. Films were spun from chloroform onto ITO coated glass substrates (1000 rpm, 5 mg/mL). An Ivium CompactStat potentiostat was used to control the electrochemical potential of the p(g2T-TT) film in a 3-electrode configuration (chronoamperometry) using identical counter and reference electrodes described above. The electrochemical potential of the film (working electrode) was increased in 50 mV steps, and the difference between subsequent absorption spectra gives the charge modulated spectra which was then fit to the Spano model.³¹ Details regarding fitting of the spectra can be found in Supplementary Note 2.

NMR measurements: ^1H and ^{19}F PFG-NMR experiments, characterizing cation (EMIM^+) and anion (TFSI^-) self-diffusion, respectively, were performed at a field strength of 9.4 T using a 400 MHz Bruker NEO spectrometer and a Bruker 5 mm water-cooled double-resonance broadband diffusion (diffBB) probe, which was equipped with z-axis gradient capabilities permitting a maximum gradient strength of 17 T/m and variable-temperature control. A standard stimulated-echo sequence (diffSte) using sine-bell magnetic field gradient pulses was employed, wherein only the gradient strength was varied for each measurement; spoiler gradient pulses of 2 ms and a longitudinal eddy current delay (LED) period of 20 ms were used for all experiments. Additionally, dummy gradient pulses were performed prior to the first spectral acquisition. Neat EMIM:TFSI was loaded and measured in a standard 5 mm NMR tube (Wilmad). The p(g2T-TT) sample was first drop cast from solution onto a sacrificial layer as described above. The film (comprising ~ 1 mg of material) was then transferred and rolled onto a coaxial NMR insert (Wilmad) to orient the lamellae of the polymer along the pulsed field gradient axis (z-axis). Ionic liquid was introduced to the film via dip coating in a solution of EMIM:TFSI, and excess surface liquid was removed via a Kimwipe. The insert was then placed in a standard 5 mm NMR tube for PFG-NMR measurements. Typical ^1H and ^{19}F PFG parameters, such as gradient pulse length (δ), diffusion time (Δ), and maximum gradient strength (g) for the neat ionic liquid (EMIM:TFSI) sample were as follows: $\delta = 2$ ms, $\Delta = 20$ ms, $g = 4$ T/m (^1H); $\delta = 2$ ms, $\Delta = 20$ ms, $g = 5$ T/m (^{19}F). Typical ^1H and ^{19}F PFG parameters for the p(g2T-TT) sample were as follows: $\delta = 2.5$ ms, $\Delta = 8$ ms, $g = 15.3$ T/m (^1H); $\delta = 1.5$ ms, $\Delta = 20$ ms, $g = 12$ T/m (^{19}F). All measurements were performed at a calibrated sample temperature of 25°C. Temperature and pulsed field gradient strength calibrations were performed with a standard consisting of 80%

ethylene glycol in DMSO-d6 (Cambridge Isotope Labs). Data were processed and analyzed in Bruker TopSpin 4.1 and Bruker Dynamics Center.

Data Availability: All the data supporting the findings of this study are available within the article, its Supplementary Information, or from the corresponding authors upon reasonable request. Source data are provided with this paper.

Methods-only References:

46. Giovannitti, A. *et al.* Controlling the mode of operation of organic transistors through side-chain engineering. *Proc. Natl. Acad. Sci. U. S. A.* **113**, 12017–12022 (2016).
47. Ashiotis, G. *et al.* The fast azimuthal integration Python library: PyFAI. *J. Appl. Crystallogr.* **48**, 510–519 (2015).
48. Dane, T. G. pygix. <https://github.com/tgdane/pygix> (2017).